Journal of Power Sources 286 (2015) 510–525

Contents lists available at ScienceDirect

Journal of Power Sources

journal homepage: www.elsevier.com/locate/jpowsour

Simplification of pseudo two dimensional battery model using dynamic profile of lithium concentration

Paulo Kemper [a], Shengbo Eben Li [b], Dongsuk Kum [a, *]

[a] The Cho Chun Shik Graduate School for Green Transportation, Korea Advanced Institute of Science and Technology (KAIST), Daejeon 305-701, South Korea
[b] Department of Automotive Engineering, Tsinghua University, Beijing 100084, Peoples Republic of China

HIGHLIGHTS

- Developed a simplified P2D model that predicts the lithium concentration gradient.
- The dynamic lithium concentration profile is rigorously derived from the P2D model.
- The voltage and concentration RMS errors are reduced up to 74% compared to the SPM.
- The proposed model is utilized to predict the localized lithium plating.

ARTICLE INFO

Article history:
Received 22 October 2014
Received in revised form
2 February 2015
Accepted 22 March 2015
Available online 24 March 2015

Keywords:
Simplified pseudo-two dimensions
Pseudo-two dimensions model
Battery management systems
Electrochemistry battery model
Model order reduction

ABSTRACT

A sophisticated BMS often requires an accurate yet simple battery model. Simplified models such as the single particle model (SPM), however, provide limited insight because lithium concentration variations over the cell thickness dimension are often neglected. In this study, we propose a simplified electrochemical model that, by reviving the lithium concentration variation across the cell thickness, provides significantly improved prediction power over the SPM. The lithium concentration profiles are first derived according to the electrochemistry-based pseudo-two dimensions (P2D) model under the steady-state assumption, they are then relaxed into a dynamic model. By employing steady-state concentration profiles coupled with averaged dynamics, the proposed model predicts electrolyte and solid surface concentrations (c_e and c_{ss}, respectively) and potential variations across the cell during both transients and stead-state conditions. The proposed model is validated by comparing the cell voltage, c_e, and c_{ss} concentration RMS errors with respect to the P2D model under pulse and constant current inputs. The simulation shows that the proposed model achieves at least 74%, 77%, and 65% RMS error reductions for cell voltage, c_{ss} and c_e, respectively, when compared to SPM in constant current simulation. Finally, the presented model is used to predict and detect local lithium plating, which the SPM is not capable of doing; our method yields predictions similar to those of the original P2D model at computational loads comparable to SPM.

1. Introduction

Batteries are vital components for mobile electrical applications such as mobile phones and electric automobiles, which need to be unplugged from a power grid for long spans of time [1]. Lithium-ion batteries, in particular, sport an attractive compromise of power density, energy density, low self-discharge rate, battery life, and cost, which makes them one of the most popular chemistry choices for unplugged applications. However, electrochemical energy storage devices usually have safety boundaries that are impractical, if not impossible, to measure in real-world applications [2]. To ensure safe, prolonged, and reliable operations, significant research effort has been put into understanding, modeling, and predicting the key limiting phenomena, which has led to various battery models with different levels of complexity and prediction capabilities (Fig. 1).

Empirical models usually populate the lower computational complexity area [3]. Their performance is satisfactory within the range of experiments used to fit their parameters, but quickly

* Corresponding author.
E-mail addresses: p-k-f@kaist.ac.kr (P. Kemper), lishbo@tsinghua.edu.cn (S.E. Li), dskum@kaist.ac.kr (D. Kum).

http://dx.doi.org/10.1016/j.jpowsour.2015.03.134
0378-7753/

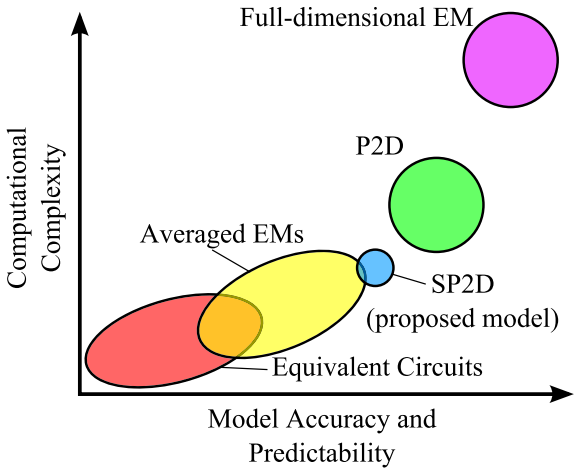

Fig. 1. Conceptual comparison of different models with respect to their complexity and prediction power.

degrades as the cell is forced outside of the expected usage scenarios [4]. Equivalent Circuit Models (ECMs) are the most popular choice of empirical models. ECMs use lumped-parameter circuit elements, e.g. inductors, resistors, and capacitors, to represent battery dynamics, where these lumped-parameters are frequently described by empirical functions of SoC and temperature. This type of model is structurally simple and computationally efficient, and has been widely studied for SoC estimation, SoH prediction, etc. However, cumulative measurement errors, capacity degradation through usage life, environmental parameter variation, and device sensitivity to initial conditions heavily affect on-board performance [5–7]. Another issue is that, for a significant portion of empirical models, their states lack physical significance, i.e. they focus on abstractions towards lumped circuit elements based on perceived macroscopic behaviors rather than on the physical interactions among the elements on a microscopic scale. These models are then oblivious to potentially dangerous phenomena that can reduce battery life or even irreversibly damage it, such as when portions of the cell during charging could be undergoing lithium plating while the cell, in the average sense, is still respecting the suggested safety operation limits [2,4]. Lack of physical significance may also considerably limit their adaptiveness, and an exponentially-growing fitting space is often required to cope with more parameters [3,4].

At the opposite corner of the complexity/predictability plane there are electrochemical models (EM). These models usually account for lithium ion intercalation and diffusion in electrodes and electrolytes, various side-reactions, double-layer effects, and lithium concentration variations across the electrode layer, which are governed by first-principle physicals laws. One of the most widely known electrochemical models is the pseudo-two dimension (P2D) model, in which the solid diffusion is calculated inside virtual particles and the electrolyte diffusion is considered only across the cell thickness. Such models often lead to complex mathematics, which are comprised of partial differential equations (PDE) and algebraic equations. As a result, the electrolyte/solid potentials as well as the electrolyte/solid concentration can be calculated across the cell with significant accuracy. The unparalleled prediction abilities of the electrochemical models, however, are shadowed by the sheer number of states; this situation translates into significant computational resources needed to properly solve PDEs.

If the computational environment is limited but information is needed in real-time, which is usually the case for practical BMS applications, it is often necessary to tackle the computational overhead. Efforts to reduce the burden of solving the electrochemical equations have relied either on mathematical manipulation (e.g. polynomial approximation [8–11] and proper orthogonal decomposition [12]) or on simplifying assumptions (e.g. volume averaged models [13], averaged models [14–16], and a particularly popular subclass of averaged models called Single Particle Models – SPM [4,17]). These assumptions, however, are likely to hamper the prediction capabilities to the point that they offer no practical advantages over empirical models.

The loss of lithium concentration and potential gradient across the cell thickness dimension is a major drawback of the averaged models (SPM included). Recent efforts into obtaining gradients across the cell with simplified models do exist. Rahimian [10] and Han [11] used a polynomial approximation to calculate electrolyte concentration variation, but no attempt was made to address the solid concentration variation (Ref. [11] addresses only its effects through the open-circuit potential distribution). Both included polynomial coefficients arbitrarily and some of these need to be solved for each point in time, which incurs additional computational effort. Luo's contribution [18] addresses the potential variations across the cell, together with pore-wall flux variations. These ideas are insightful for some BMS functions (e.g. lithium plating prediction), but they offer no information about the concentration of lithium, which is necessary for ensuring cell safety. While [10] is an averaged model with an increased number of states, the contribution of [11], which provides some insight into concentration variations, requires multiple particles. That is also the case for [18], whose model actually requires three representative particles per electrode.

One critical problem arising from the lack of gradient knowledge is localized lithium plating, which is usually seen at boundaries and results in capacity losses as well as other safety concerns [19,20]. The lithium plating tends to occur during recharge at high SOC, and at low temperatures or high currents; without such gradient knowledge the BMS would have to employ a conservative control strategy in order to avoid localized lithium plating [3,4]. These problems are particularly important for large cells because they become more pronounced as the cell thickness increases [4], which in turn must be carefully considered during the cell design process. Therefore, a simplified EM that can predict concentration gradients with reduced computational load is necessary.

Aiming to provide a model with a computational burden equivalent to that of average models but with prediction capabilities similar to that of P2D, the Simplified P2D (SP2D) model was conceived. The main contribution of the SP2D is to provide a physics-based concentration profile, derived from the P2D model, coupled with electrolyte averaged dynamics, in order to recover the concentration gradients across the thickness dimension. The existence of these dynamic concentration profiles is the key difference between the SP2D and other averaged models. Knowing the concentration across the cell provides a basis for predicting much more accurate safety boundaries as well as other BMS functions and enables the design of studies with reduced computational burden.

The remainder of this paper is organized as follows: Section 2 introduces the first-principle model used as a base for the SP2D; the derivation of SP2D is presented in Section 3; Section 4 provides the model validation versus a higher-order EM, and also a comparison with SPM; Localized lithium plating prediction is presented in Section 5; and the concluding remarks and future work can be found in Section 6.

2. Electrochemical model – P2D

The pseudo-two dimensions (P2D) model is one of the most accurate and detailed electrochemical models that was developed

based on the electrochemistry first-principles and has been validated for a broad range of lithium chemistries and input current densities [21]. Thus, this work will use P2D as the starting point for further model development.

The P2D is a galvanostatic, isothermal electrochemical model [4,21–24]. That is, the dynamics arising from changes in current are assumed to be negligible, and the cell is kept at a constant temperature. The key assumption for P2D model is that the conductivity of current collectors is so high that there is no significant variations over the current collector space (y and z), and thus the one dimensional (x) chemical reaction dynamics dominates the cell dynamics. In addition, to account for the intercalation/de-intercalation of lithium on the solid matrix and the diffusion on electrolyte over a single dimension, small spherical solid particles are conceptually superimposed with the electrolyte. These particles are considered to exist at every position inside the electrode domains and lithium is stored inside of them. The diffusion of lithium inside of these particles is calculated over the pseudo-dimension r, the radius of such particle. Thus, this model in which only one spatial dimension (x) and a pseudo-dimension (r) are considered is known as Pseudo Two Dimension (P2D). Fig. 2 depicts the three domains inside of a battery cell: negative electrode, electrolyte and positive electrode.

2.1. Cell voltage

The cell voltage is defined as being the difference between the potential at the negative and positive current collectors:

$$V_{cell}(t) = \Phi_s\left(0^+, t\right) - \Phi_s\left(0^-, t\right) \tag{1}$$

Using the Butler–Volmer's definition of overpotential and rearranging the terms, we have that the potential on the electrode is:

$$\Phi_s(x,t) = \mathscr{U}(c_{ss}(x,t)) + \Phi_e(x,t) + \eta_s(x,t) + \Omega(x,t) \tag{2}$$

The open-circuit potential $\mathscr{U}(c_{ss})$ is usually an empirical relationship which depends on the cell chemistry and concentration of lithium at the particle surface $(c_{ss}(x,t) \triangleq c_s(x,R_p,t))$. The Ohmic losses are modeled as $\Omega(x,t) = FRfj_n(x,t)$.

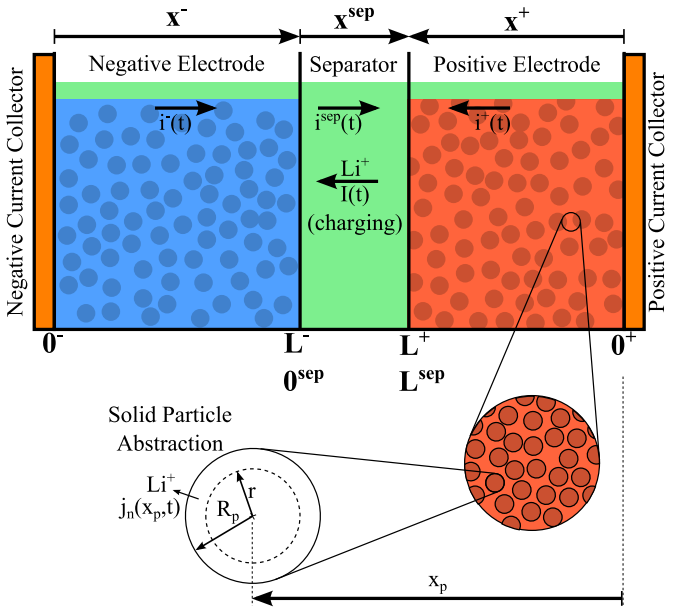

Fig. 2. The three domains inside of a Lithium-Ion cell. The input current $I(t)$ arrow denotes the flow of lithium ions, and it is positive when charging. Likewise, the pore-wall flux density j_n is positive when lithium ions are departing the particle.

2.2. Butler–Volmer kinetics

The overpotential is obtained solving the Butler–Volmer equation:

$$j_n(x,t) = \frac{i_0(x,t)}{F}\left[\exp\left(\frac{\alpha_a F}{RT}\eta_s(x,t)\right) - \exp\left(-\frac{\alpha_c F}{RT}\eta_s(x,t)\right)\right] \tag{3}$$

where the exchange current density is defined as:

$$i_0 = Fk_{eff}[c_e(x,t)]^{\alpha_a}[c_{ss}(x,t)]^{\alpha_c}\left[c_s^{max} - c_{ss}(x,t)\right]^{\alpha_a} \tag{4}$$

Taking both transfer coefficients α_a and α_c to be equal to 0.5 [4,8,10], (3) can be simplified to:

$$\begin{aligned} j_n(x,t) &= \frac{i_0(x,t)}{F}\left[\exp\left(\frac{F}{2RT}\eta_s(x,t)\right) - \exp\left(-\frac{F}{2RT}\eta_s(x,t)\right)\right] \\ j_n(x,t) &= \frac{i_0(x,t)}{F}\sinh\left(\frac{F}{2RT}\eta_s(x,t)\right) \\ \eta_s(x,t) &= \frac{2RT}{F}\operatorname{arcsinh}\left(\frac{Fj_n(x,t)}{i_0(x,t)}\right) \end{aligned} \tag{5}$$

and (4) becomes:

$$i_0 = Fk_{eff}\sqrt{c_e(x,t)c_{ss}(x,t)\left(c_s^{max} - c_{ss}(x,t)\right)} \tag{6}$$

2.3. Conservation of charge

To ensure charge conservation, the pore-wall flux density $j_n(x,t)$ is related to the electrolyte current $i_e(x,t)$ according to:

$$\frac{\partial i_e(x,t)}{\partial x} = aFj_n(x,t) \tag{7}$$

where $a = 3(1-\varepsilon-\varepsilon_f)/R_p$.

2.4. Electrode and electrolyte potentials

The relationship of electrolyte current with electrode potential (Ohm's law) is defined, taking $\sigma = \sigma_\infty(1-\varepsilon-\varepsilon_f)^{1.5}$, as:

$$\frac{\partial \Phi_s(x,t)}{\partial x} = \frac{i_e(x,t) - i(t)}{\sigma} \tag{8}$$

The electrolyte potential is defined, taking $\kappa = \kappa_\infty\varepsilon^{1.5}$, as:

$$\frac{\partial \Phi_e(x,t)}{\partial x} = -\frac{i_e(x,t)}{\kappa} + \frac{2RTt_a^0}{F}\left(\frac{\partial \ln c_e(x,t)}{\partial x}\right) \tag{9}$$

2.5. Lithium diffusion on electrode and electrolyte

To complete the model, the dynamics of lithium on the solid electrode and electrolyte are represented by the following equations:

$$\frac{\partial c_s(x,r,t)}{\partial t} = \frac{1}{r^2}\frac{\partial}{\partial r}\left(D_s r^2 \frac{\partial c_s(x,r,t)}{\partial r}\right) \tag{10}$$

$$\frac{\partial c_e(x,t)}{\partial t} = \frac{\partial}{\partial x}\left(D_e \frac{\partial c_e(x,t)}{\partial x}\right) + \frac{t_a^0}{F\varepsilon}\frac{\partial i_e(x,t)}{\partial x} \tag{11}$$

2.6. Boundary and initial conditions

Lastly, to solve the model composed by equations (1)–(11), the following initial conditions (13) and (14) and boundary conditions (15)–(24) are introduced:

$$i^+(t) = -i^-(t) = -i^{sep}(t) = I(t) \tag{12}$$

$$c_s(x,r,0) = c_{s0} \tag{13}$$

$$c_e(x,0) = c_{e0} \tag{14}$$

$$i_e\left(0^+,t\right) = i_e\left(0^-,t\right) = 0 \tag{15}$$

$$-i_e\left(L^+,t\right) = i_e\left(L^-,t\right) = i_e(x^{sep},t) = I(t) \tag{16}$$

$$\Phi_e\left(0^+,t\right) = 0 \tag{17}$$

$$\Phi_e\left(L^+,t\right) = \Phi_e(L^{sep},t);\ \Phi_e\left(L^-,t\right) = \Phi_e(0^{sep},t) \tag{18}$$

$$\left.\frac{\partial c_e}{\partial x}\right|_{x=0^+} = \left.\frac{\partial c_e}{\partial x}\right|_{x=0^-} = 0 \tag{19}$$

$$\varepsilon^+\left(D_e^+\frac{\partial c_e}{\partial x}\right)\Big|_{x=L^+} = -\varepsilon^{sep}\left(D_e^{sep}\frac{\partial c_e}{\partial x}\right)\Big|_{x=L^{sep}} \tag{20}$$

$$\varepsilon^-\left(D_e^-\frac{\partial c_e}{\partial x}\right)\Big|_{x=L^-} = \varepsilon^{sep}\left(D_e^{sep}\frac{\partial c_e}{\partial x}\right)\Big|_{x=0^{sep}} \tag{21}$$

$$c_e\left(L^+,t\right) = c_e(L^{sep},t);\quad c_e\left(L^-,t\right) = c_e(0^{sep},t) \tag{22}$$

$$\left.\frac{\partial c_s(x,r,t)}{\partial r}\right|_{r=0} = 0 \tag{23}$$

$$\left.\frac{\partial c_s(x,r,t)}{\partial r}\right|_{r=R_p} = -\frac{1}{D_s}j_n(x,t) \tag{24}$$

3. Simplified pseudo-two dimensions model

The objective of this section is to develop a simplified (reduced-order) model that can predict the lithium concentration variations across the cell. That is, a model with similar prediction capabilities from P2D but with reduced computational burden. The process will include the following assumptions:

1. The following cell parameters variation across the thickness dimension is negligible or results in negligible effects: ε, t_a (both already assumed so for the presented P2D), κ, and D_e. Depending on the chosen electrolyte, the variations of κ and D_e may induce noticeable error;
2. At steady-state, the pore-wall flux density variation across the thickness dimension is negligible (refer to Fig. 3a). This is true for small to moderate current densities or for thin electrodes;
3. The side reactions have negligible impact;
4. The average electrolyte diffusion, i.e. the dynamics of bulk electrolyte concentration, can be modeled by a system of linear ODEs;
5. The solid surface concentration (c_{ss}) profile is similar in shape of the electrolyte concentration (c_e) profile. This is expected to hold at most times since lithium is exchanged with the electrolyte through the SEI, thus c_e and c_{ss} should have a similar distribution, but not necessarily similar magnitudes (refer to Fig. 3b and c);
6. The c_e and c_{ss} profiles derived for steady-state also hold for transients

The final goal is to obtain a solid concentration profile on the following format (Fig. 3c):

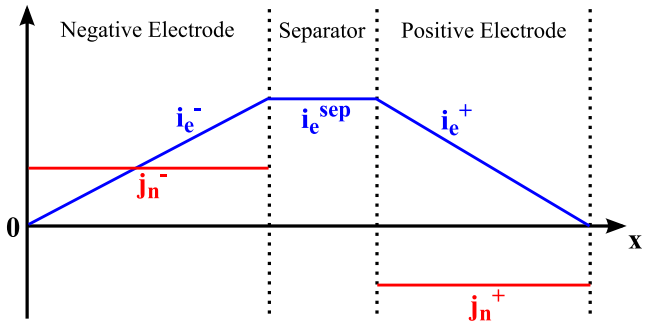

(a) Simplified $j_n(x)$ and resulting $i_e(x)$ at steady state

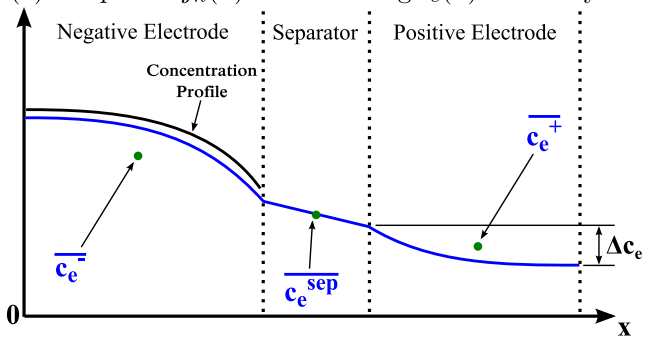

(b) Electrolyte concentration at steady state

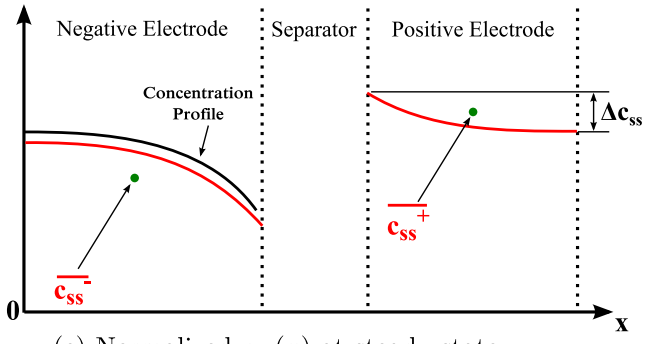

(c) Normalized $c_{ss}(x)$ at steady state

Fig. 3. Visual depiction of some assumptions used in the model derivation, and the c_e and c_{ss} profile components.

$$\widehat{c_{ss}}(x,t) = \overline{c_{ss}}(t) + g(x)h\left(\overline{c_{ss}}(t), \overline{c_e}(t)\right) \quad (25)$$

In (25) $g(x)$ is the profile shape, based on the electrolyte profile,[1] and $h(\overline{c_{ss}}(t), \overline{c_e}(t))$[2] is the profile magnitude, which depends on average solid surface concentration and bulk electrolyte concentration. The derivation of the model is summarized as follows:

1. Derive the steady-state electrolyte lithium concentration profile from the P2D model
2. Derive a steady-state relationship between the electrolyte concentration variation and the solid surface concentration variation across the cell thickness
3. Relax the steady-state assumption by deriving electrolyte averaged dynamic equations from P2D and relaxed steady-state model
4. Find an algebraic relationship between solid surface concentration, averaged surface concentration, and averaged electrolyte concentration

The process above was devised to avoid the use of arbitrary concentration profiles (e.g. the parabolic profiles of Refs. [10] or [11]) and to reduce the deleterious effects of using averaging assumptions to simplify the model development (e.g. the single particle assumption which completely removes electrolyte concentration variation). The main difference between the above process and the derivation of averaged models (SPM included) is that the averaged concentration values[3] ($\overline{c_e}(t)$ and $\overline{c_{ss}}(t)$) are used to estimate the concentration across the cell thickness ($\widehat{c_e}(x,t)$ and $\widehat{c_{ss}}(x,t)$) instead of just assuming negligible variation across the space and time. Accounting for these intra-cell variations allows an advanced BMS to use the cells closer to its limits without posing a safety threat to the battery [2,4]. Another advantage of this approach is that the averaged electrolyte concentration dynamics and the averaged solid concentration dynamics are decoupled, which enables faster computation of the whole model without significant loss of accuracy at low frequencies, when compared to the P2D.

3.1. Electrolyte lithium concentration profile at steady-state

Equation (11), at steady-state,[4] becomes:

$$\frac{\partial}{\partial x}\left(D_e\frac{\partial c_e(x)}{\partial x}\right) = -\frac{t_a^0}{F\varepsilon}\frac{\partial i_e(x)}{\partial x}$$

Then, performing indefinite integration:

$$\int \frac{\partial}{\partial x}\left(D_e\frac{\partial c_e(x)}{\partial x}\right)dx = -\int \frac{t_a^0}{F\varepsilon}\frac{\partial i_e(x)}{\partial x}dx$$

$$D_e\frac{\partial c_e(x)}{\partial x} = -\frac{t_a^0}{F\varepsilon}i_e(x) + C$$

Using the boundary conditions and Assumption 1, $C = 0$:

$$D_e\frac{\partial c_e(x)}{\partial x} = -\frac{t_a^0}{F\varepsilon}i_e(x) \quad (26)$$

At the separator, $i_e^{sep}(x) = i^{sep}$ by definition. Thus, for the separator (26) becomes:

$$D_e\frac{\partial c_e^{sep}(x)}{\partial x} = -\frac{t_a^0}{F\varepsilon^{sep}}i^{sep} \quad (27)$$

For the electrodes, the value of $i_e(x)$ could be calculated using (7), as it is performed in the P2D, but this effectively couples the electrolyte and solid diffusion dynamics. Instead, Assumption 2 states that at steady-state $(\partial/\partial x)j_n(x) \approx 0$, leading to:

$$\int \frac{\partial}{\partial x}j_n(x)dx = j_n(x) = \overline{j_n} = \frac{i}{LaF}$$

$$\int \frac{\partial}{\partial x}i_e(x)dx = \int aFj_n(x)dx = \int \frac{1}{L}idx$$

$$i_e(x) = \frac{1}{L}xi$$

In the above equation, the integration constant is zero, based on the boundary condition (15) or (16), and was thus omitted. Then, for the electrodes, (26) becomes:

$$D_e\frac{\partial c_e(x)}{\partial x} = -\frac{t_a^0}{F\varepsilon L}xi \quad (28)$$

Using Assumption 1 and performing indefinite integration in (27) and (28):

$$\int D_e\frac{\partial c_e^{sep}(x)}{\partial x}dx = -\int \frac{t_a^0}{F\varepsilon^{sep}}i^{sep}dx$$

$$c_e^{sep}(x) = -\frac{t_a^0}{D_eF\varepsilon^{sep}}xi^{sep} + C_2^{sep} \quad (29)$$

and

$$\int D_e\frac{\partial c_e(x)}{\partial x}dx = -\int \frac{t_a^0}{F\varepsilon L}xidx$$

$$c_e(x) = -\frac{t_a^0}{2D_eF\varepsilon L}x^2i + C_2 \quad (30)$$

In order to calculate the value of the integration constants C_2^+, C_2^{sep} and C_2^-, the boundary condition (22) will be used. In addition, using Assumption 3, the total amount of lithium ions in the electrolyte is constant, i.e.:

$$\frac{\varepsilon^+L^+\overline{c_e^+}(t) + \varepsilon^{sep}L^{sep}\overline{c_e^{sep}}(t) + \varepsilon^-L^-\overline{c_e^-}(t)}{\varepsilon^+L^+ + \varepsilon^{sep}L^{sep} + \varepsilon^-L^-} = c_e^0 \quad (31)$$

We proceed to calculate the average electrolyte concentrations by averaging (29 and 30) across space, and then put the results together with (22) and (31). Lastly, the integration constants can be identified to be in the following form:

$$C_2 = \frac{t_a^0}{2D_eF}\gamma i(t) + c_e^0$$

where, in order to obtain shorter formulas, we define the geometric proportionality constant γ as:

$$\gamma^+ = \frac{2L^{sep}\varepsilon^+ + L^+\varepsilon^{sep}}{\varepsilon^+\varepsilon^{sep}} - \gamma^{sep}$$

[1] Assumption 5.
[2] Δc_{ss} in Fig. 3c.
[3] In this work, a bar stands for "averaged quantity", whereas a hat denotes "estimated quantity".
[4] The steady-state variables will not include the t term in order to explicitly represent their lack of temporal dependency.

$$\gamma^{sep} = \frac{2L^{sep}\left(L^{+}\varepsilon^{+} + L^{sep}\varepsilon^{sep}\right)}{3\varepsilon^{sep}\left(L^{+}\varepsilon^{+} + L^{sep}\varepsilon^{sep} + L^{-}\varepsilon^{-}\right)}$$

$$\gamma^{-} = \frac{L^{-}}{\varepsilon^{-}} + \gamma^{sep}$$

Then finally the steady-state electrolyte concentration equations (29) and (30) can be re-written as:

$$c_e^{+}(x) = \frac{t_a^0}{2D_eF}\left(\gamma^{+} - \frac{x^2}{\varepsilon^{+}L^{+}}\right)i^{+} + c_e^0 \tag{32}$$

$$c_e^{sep}(x) = \frac{t_a^0}{2D_eF}\left(\gamma^{sep} - \frac{2x}{\varepsilon^{sep}}\right)i^{sep} + c_e^0 \tag{33}$$

$$c_e^{-}(x) = \frac{t_a^0}{2D_eF}\left(\gamma^{-} - \frac{x^2}{\varepsilon^{-}L^{-}}\right)i^{-} + c_e^0 \tag{34}$$

3.2. Solid surface profile magnitude

In order to obtain the solid surface concentration profile magnitude (i.e. $h(\overline{c_{ss}}(t), \overline{c_e}(t))$ in (25)), it is necessary to find a relationship between the electrolyte concentration at the electrode surface and the electrolyte. To do so, instead of evaluating the formulas for every x, the Δ of c_{ss} and c_e will be used. In this work, Δ of a function/variable is defined as:

$$\Delta f(t) = f(L,t) - f(0,t)$$

Using the above definition, we can easily calculate the Δc_e for each electrode at steady-state[5] as:

$$\Delta c_e = -\frac{t_a^0 L}{2D_eF\varepsilon}i \tag{35}$$

In order to calculate Δc_{ss}, the derivation starts from (26). However, differently from the previous section, instead of assuming linear $i_e(x)$ (Assumption 2), (8) will be used to remove the electrolyte current for this derivation. It results in:

$$D_e\frac{\partial c_e(x,t)}{\partial x} = -\frac{t_a^0}{F\varepsilon}\left(i(t) + \sigma\frac{\partial \Phi_s}{\partial x}\right) \tag{36}$$

Performing indefinite integration on (36):

$$\int D_e\frac{\partial c_e(x)}{\partial x}dx = -\int \frac{t_a^0}{F\varepsilon}\left(i + \sigma\frac{\partial \Phi_s}{\partial x}\right)dx$$

$$c_e(x) = -\frac{t_a^0}{D_eF\varepsilon}(xi + \sigma\Phi_s) + C_3 \tag{37}$$

Note that C_3 will vanish when the Δ operator is applied to find Δc_e. Evaluating Δc_e based on (37):

$$\Delta c_e = -\frac{t_a^0}{D_eF\varepsilon}(Li + \sigma\Delta\Phi_s) \tag{38}$$

where

$$\Delta\Phi_s = \Delta\mathscr{U}(c_{ss}) + \Delta\Phi_e + \Delta\eta_s + \Delta\Omega$$

Now, (9) is evaluated using (8) (refer to Appendix A), leading to:

$$\Delta\Phi_e = \frac{-Li(t) - \sigma(\Delta\eta_s + \Delta\mathscr{U}(c_{ss}) + \Delta\Omega) + 2RTt_a^0F^{-1}\Delta\ln c_e}{\overline{\kappa} + \sigma} \tag{39}$$

To shorten the formulas, let us define $\Delta\Sigma(c_{ss},c_e)$ as:

$$\Delta\Sigma(c_{ss},c_e) = \Delta\eta_s + \Delta\mathscr{U}(c_{ss}) + \Delta\Omega + 2RTt_a^0F^{-1}\overline{\kappa}^{-1}\Delta\ln c_e$$

And plugging (39) into (38), it yields:

$$\Delta c_e = -\frac{t_a^0\overline{\kappa}}{D_eF\varepsilon}\left(\frac{Li + \sigma\Delta\Sigma(c_{ss},c_e)}{\overline{\kappa} + \sigma}\right) \tag{40}$$

Since (35) and (40) should be equivalent:

$$-\frac{t_a^0 L}{2D_eF\varepsilon}i = -\frac{t_a^0\overline{\kappa}}{D_eF\varepsilon}\left(\frac{Li + \sigma\Delta\Sigma(c_{ss},c_e)}{\overline{\kappa} + \sigma}\right)$$

$$\Delta\Sigma(c_{ss},c_e) = \frac{L(\sigma - \overline{\kappa})}{2\overline{\kappa}\sigma}i \tag{41}$$

Equation (41) relates the steady state values of the boundary potentials in $\Delta\Sigma(c_{ss},c_e)$ with the current density magnitude applied to the cell. The objective, however, is to relate the profile magnitude to the average concentrations $\overline{c_{ss}}(t)$ and $\overline{c_e}(t)$, but not to the current density magnitude. This issue will be tackled by the following sections.

In addition, the value of each component of $\Delta\Sigma(c_{ss},c_e)$ is not particularly interesting for this model development, and its evaluation may become burdensome for online model evaluation. Instead, this relationship can be calculated offline to generate a lookup table to be used in applications with limited computational power.

3.3. Averaged lithium diffusion on electrolyte

Aiming to relax the steady-state assumption, (32)–(34) will be first volume-averaged to obtain the averaged electrolyte concentration steady-state value, using the following process:

$$\frac{1}{L}\int_0^L f(x,t)dx = \overline{f}(t)$$

$$\overline{c_e^{+}} = \frac{t_a^0}{2D_eF}\left(\gamma^{+} - \frac{L^{+}}{3\varepsilon^{+}}\right)i^{+} + c_e^0 \tag{42}$$

$$\overline{c_e^{sep}} = \frac{t_a^0}{2D_eF}\left(\gamma^{sep} - \frac{L^{sep}}{\varepsilon^{sep}}\right)i^{sep} + c_e^0 \tag{43}$$

$$\overline{c_e^{-}} = \frac{t_a^0}{2D_eF}\left(\gamma^{-} - \frac{L^{-}}{3\varepsilon^{-}}\right)i^{-} + c_e^0 \tag{44}$$

Based on Assumption 4, the average diffusion behaves like a linear ODE system with $i(t)$ as input. It is then expected that the steady state value is directly proportional to the input. With that in mind, (42–44) are re-arranged as:

$$\left(\overline{c_e^{+}} - c_e^0\right)\left(\gamma^{+} - \frac{L^{+}}{3\varepsilon^{+}}\right)^{-1} = \frac{t_a^0}{2D_eF}i^{+} \tag{45}$$

[5] Again, suppressing the t for steady-state variables.

$$\left(\overline{c_e^{sep}} - c_e^0\right)\left(\gamma^{sep} - \frac{L^{sep}}{\varepsilon^{sep}}\right)^{-1} = \frac{t_a^0}{2D_eF} i^{sep} \tag{46}$$

$$\left(\overline{c_e^-} - c_e^0\right)\left(\gamma^- - \frac{L^-}{3\varepsilon^-}\right)^{-1} = \frac{t_a^0}{2D_eF} i^- \tag{47}$$

Now, plugging in (42)–(44) into (32)–(34), and using Assumption 6, (32)–(34) become[6]:

$$\widehat{c_e^+}(x,t) = \overline{c_e^+}(t)\left(\gamma^+ - \frac{x^2}{\varepsilon^+ L^+}\right)\left(\gamma^+ - \frac{L^+}{3\varepsilon^+}\right)^{-1} + c_e^0\left(\frac{3x^2/L^+ - L^+}{3\varepsilon^+}\right)\left(\gamma^+ - \frac{L^+}{3\varepsilon^+}\right)^{-1} \tag{48}$$

$$\widehat{c_e^{sep}}(x,t) = \overline{c_e^{sep}}(t)\left(\gamma^{sep} - \frac{2x}{\varepsilon^{sep}}\right)\left(\gamma^{sep} - \frac{L^{sep}}{\varepsilon^{sep}}\right)^{-1} + c_e^0\left(\frac{2x - L^{sep}}{\varepsilon^{sep}}\right)\left(\gamma^{sep} - \frac{L^{sep}}{\varepsilon^{sep}}\right)^{-1} \tag{49}$$

$$\widehat{c_e^-}(x,t) = \overline{c_e^-}(t)\left(\gamma^- - \frac{x^2}{\varepsilon^- L^-}\right)\left(\gamma^- - \frac{L^-}{3\varepsilon^-}\right)^{-1} + c_e^0\left(\frac{3x^2/L^- - L^-}{3\varepsilon^-}\right)\left(\gamma^- - \frac{L^-}{3\varepsilon^-}\right)^{-1} \tag{50}$$

Equations (48)–(50) express the estimated electrolyte concentration profile $\widehat{c_e}(x,t)$ across the cell thickness based on the averaged concentration $\overline{c_e(t)}$ and initial equilibrium concentration c_e^0. Plugging these equations in (11), the averaged concentration equations can be obtained as:

$$\frac{d}{dt}\overline{c_e^+}(x,t) = \frac{D_e}{\varepsilon^+ L^+}\left(c_e^0 - \overline{c_e^+}(x,t)\right)\left(\gamma^+ - \frac{L^+}{3\varepsilon^+}\right)^{-1} + \frac{t_a^0}{F\varepsilon^+ L^+} i^+(t) \tag{51}$$

$$\frac{d}{dt}\overline{c_e^{sep}}(x,t) = -\frac{2D_e}{L^{sep}}\left[\left(c_e^0 - \overline{c_e^+}(x,t)\right)\left(\gamma^+ - \frac{L^+}{3\varepsilon^+}\right)^{-1} + \left(c_e^0 - \overline{c_e^-}(x,t)\right)\left(\gamma^- - \frac{L^-}{3\varepsilon^-}\right)^{-1}\right] \tag{52}$$

$$\frac{d}{dt}\overline{c_e^-}(x,t) = \frac{D_e}{\varepsilon^- L^-}\left(c_e^0 - \overline{c_e^-}(x,t)\right)\left(\gamma^- - \frac{L^-}{3\varepsilon^-}\right)^{-1} + \frac{t_a^0}{F\varepsilon^- L^-} i^-(t) \tag{53}$$

The complete derivation of equations (51)–(53) can be found on Appendix B.

3.4. Defining an algebraic solid surface concentration profile

This section will conclude the definition of the target profile in (25). Based on (41), the difference between both ends of an electrode (separator and current collector) is known at steady-state. Using (45), (47) and (41), a relationship between averaged electrolyte concentration and solid surface concentration which is not dependent on current density can be obtained as follows:

$$\left(\overline{c_e}(t) - c_e^0\right)\left(\gamma - \frac{L}{3\varepsilon}\right)^{-1}\frac{2D_eF}{t_a^0} = i(t)$$

$$\Delta\Sigma(c_{ss}, c_e) = \frac{3D_eF\varepsilon L(\sigma - \overline{\kappa})}{\overline{\kappa}\sigma t_a^0(3\gamma\varepsilon - L)}\left(\overline{c_e}(t) - c_e^0\right) \tag{54}$$

Based on Assumption 5, the general shape of c_{ss} profile is quadratic (i.e. same of (32 and 34)) Then, a relationship between averaged solid surface value $\overline{c_{ss}}$, the boundary values, and the magnitude difference between both values Δc_{ss} can be found as:

$$c_{ss}(x,t)|_{x=0} = \overline{c_{ss}} - \frac{\Delta c_{ss}}{3} \tag{55}$$

$$c_{ss}(x,t)|_{x=L} = \overline{c_{ss}} + \frac{2\Delta c_{ss}}{3} \tag{56}$$

It also follows that the previously defined profile shape function $g(x)$ is equivalent to:

$$g(x) = \frac{x^2}{L^2} - \frac{1}{3} \tag{57}$$

It is a simple task to use (48–50, 54–56) to generate a lookup table (LUT) offline which takes $\overline{c_{ss}}$ and $\overline{c_e}$ as inputs. This LUT is, in fact, the previously defined function $h(\overline{c_{ss}}, \overline{c_e})$:

$$h\left(\overline{c_{ss}}, \overline{c_e}\right) = LUT\left(\overline{c_{ss}}, \overline{c_e}\right) \tag{58}$$

Plugging in (57 and 58) into (25), the solid surface concentration estimator becomes:

$$\widehat{c_{ss}}(x,t) = \overline{c_{ss}}(t) + \left(\frac{x^2}{L^2} - \frac{1}{3}\right) LUT\left(\overline{c_{ss}}(t), \overline{c_e}(t)\right) \tag{59}$$

The SP2D model derivation is concluded. Electrolyte averaged dynamics can be calculated using (51)–(53), which can be converted to a linear system by simply updating variables. Averaged solid surface concentration can be calculated using a surrogate particle, in a method similar to averaged models.[7] Then, the electrolyte concentration at the boundaries and the solid surface concentration at the boundaries can be estimated using (48)–(50) and (59), respectively. Lastly, the potentials Φ_e, η_s, Ω and $\mathscr{U}$ can be calculated using the equations developed in [25] (equations summarized on Appendix C), and then the cell potential can be obtained. This process is visually depicted in Fig. 4.

The SP2D is capable of estimating the lithium concentration distribution across space from averaged, decoupled equations. These can be used to provide better insights about future cell conditions and prevent dangerous actions with less conservative limits, further improving the capabilities of BMS [2,4] without significant computational burden added. For example, as presented in Section 5, this model can effectively improve the lithium plate prediction across the thickness dimension. Lastly, the presented model can also be an alternative to aid parameter optimization based on multiple model simulations.

[6] At this point, the time dependency is returned to the variables.

[7] It is worth mentioning that this surrogate particle diffusion could be evaluated using the original PDE (10) or some ODE approximation (e.g., the method proposed by Ref. [8]).

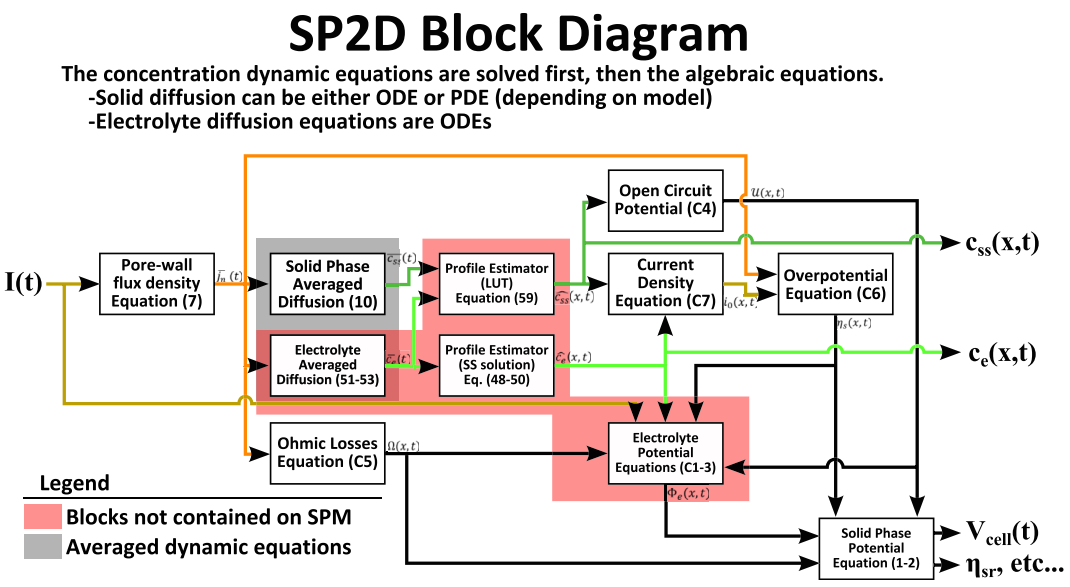

Fig. 4. Block diagram of SP2D, with highlight on the blocks which are not present on common SPMs.

4. Model validation and discussion

In order to evaluate the accuracy of the developed SP2D, two types of simulations were conducted: full discharge/charge at constant current and a pulse current profile. Due to limitations in test facilities, the model comparison was performed versus the P2D output from DualFoil 5.1 [26]. A similar validation method, i.e., against a validated higher-order model, was also used by [10,11,18]. The cell parameters can be found in Appendix E on Table E.7, and a detailed explanation of the two simulation setups follows.

4.1. During constant current

The steady state accuracy was evaluated by comparing the cell voltage error under constant current input conditions, taking the P2D output from DualFoil 5.1 [26] as the reference value. The charge/discharge currents[8] chosen for the test were ±C/4, ±C/2, ±1C, and ±2C. The simulation ended when either V_{cell}^{max} or V_{cell}^{min} thresholds were voided. For illustration purposes, Fig. 5a depicts the output voltage and the normalized RMS error of P2D and the evaluated models at full charge current of 2C. Fig. 6 plots the output voltage and the normalized RMS error of P2D and the evaluated models at full discharge current of 2C. Fig. 8a summarizes the simulation results. The detailed data can be found in Tables D.1.

Based on these plots, it is possible to notice that the cell voltage error of SP2D significantly reduces when compared to the SPM. The absolute normalized cell voltage error usually stays under 0.4% for SP2D, while the SPM goes above 1% at constant charge/discharge of 2C. While the error value is smaller at lower currents, the same trend applies. This behavior is expected, since the SP2D was designed to capture the concentration and potential gradients across the electrode, which clearly helps predicting the cell voltage and the potential difference between the two electrode boundary potentials. Nevertheless, this improvement is obtained with minimal complexity increase when compared to the SPM. The predictions of local battery behavior during constant current is important in especial for minimizing charging times while keeping the cell safe as well as better monitoring and management of the cell at quasi-constant discharge regimes such as electric vehicles cruising on a highway or stand-by loads (e.g. mobile devices).

4.2. During pulse current

The transient accuracy of SPM and SP2D is also evaluated in terms of normalized RMS error, taking the P2D output from DualFoil 5.1 [26] as the reference value. The input current profile was set as follows:

1. Define the peak discharge current density D;
2. Start cycle with discharge D for 12 s;
3. End cycle with charge D/4 for 48 s;
4. Repeat the cycle four times.

The peak discharge currents chosen for the test were C/4, C/2, 1C, 2C, and 4C, and the cell parameters can be found in Appendix E on Table E.7. A similar test setup was used in Refs. [25,27]. For illustration purposes, Fig. 7 depicts the output voltage and normalized cell voltage error of P2D, SP2D and SPM at peak discharge current of 4C. Fig. 8b summarizes the pulse simulation results. The detailed data can be found in Table D.4.

At first glance, one can notice that the SP2D cell voltage error is the largest right after a current switching event. However, as expected, the error starts to converge to near zero as time passes. This behavior is the opposite of SPM, in which the voltage error tends to increase with time. The key responsible factors for this behavior are the consideration of concentration distribution across the cell, and the electrolyte potential. The standard SPM neglects both electrode surface potential and concentration variations across the thickness dimension. In fact, it was found out that introducing only one of either the electrolyte potential or the concentration variations across the cell (or vice-versa) adds up little to the standard SPM accuracy. This is mostly because the potential variation across the electrode surface contributes for the electrolyte potential and open circuit potential, so not having either will eventually cap the prediction capabilities. However, when both of these features are present, a significant accuracy improvement is obtained.

The SP2D large error at switching is originated from two factors: concentration profile derivation based on steady-state, and profile based on averaged quantities ($\overline{c_{ss}}$ and $\overline{c_e}$). The averaged dynamics

[8] In this work, based on the cell parameters, 1C is defined as 40 A m^{-2}.

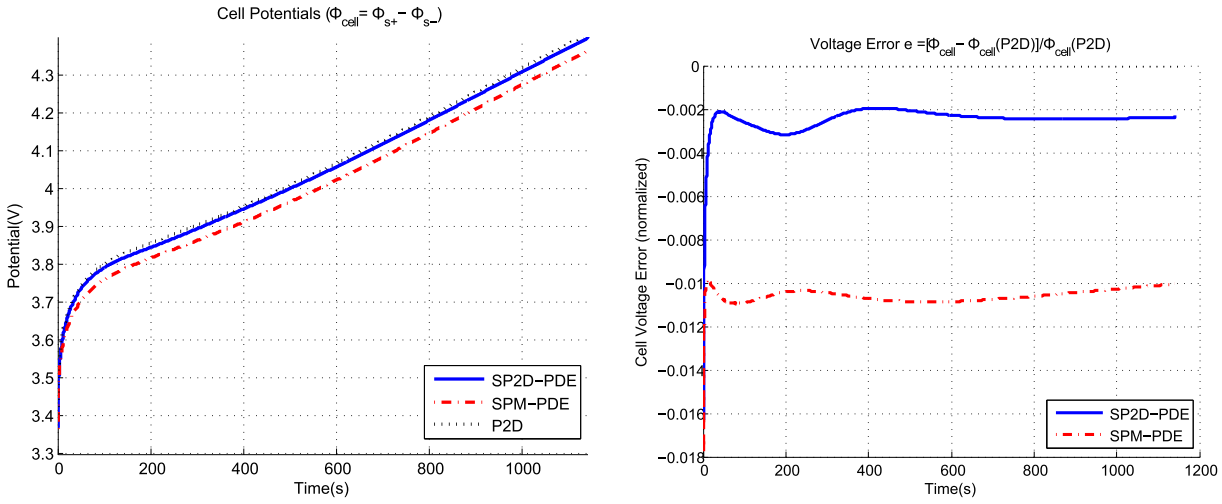

(a) Cell Voltage (b) Normalized Voltage Error

Fig. 5. Voltage output and normalized voltage error of the SPM-PDE and SP2D-PDE versus the P2D at 2C full charge.

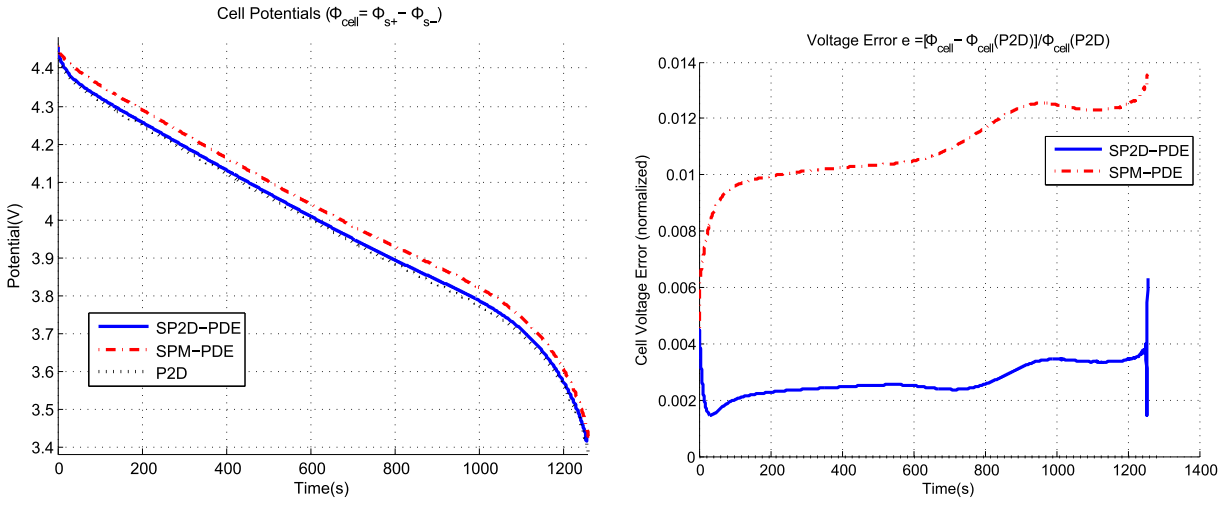

(a) Cell Voltage (b) Normalized Voltage Error

Fig. 6. Voltage output and normalized voltage error of the SPM-PDE and SP2D-PDE versus the P2D at 2C full discharge.

will behave, by definition, slower than some of the points inside of the cell, while the steady-state derivation is a design choice which is naturally void at the transient state right after current switching. One possible way to mitigate this issue is to add a dynamic state to the profiles, but linking such a state to a physical parameter is a challenge on itself. Nevertheless, if the current switching magnitude is not very large or not very frequent, the error will soon converge to near zero, which is a desired trait. It is important to notice that the SP2D is an open-loop model: its error will not necessarily converge to zero. Further error reduction could be accomplished by using the presented model with closed-loop techniques.

4.3. Concentration values at boundaries

Since the goal of this model is to accurately represent the lithium distribution across space (the cell thickness), it is also important to evaluate the prediction accuracy of this feature. To do so, the total normalized concentration RMS error at each of the four boundaries (i.e. 0^-, L^-, L^+ and 0^+, refer to Fig. 2) is evaluated and summed. This measurement is performed both for solid surface and electrolyte concentrations. Mathematically, this can be expressed as:

$$RMS_{ss}^{model}(x) = \sqrt{\frac{1}{n}\sum_{n}\left(\frac{c_{ss}^{model}(x_n) - c_{ss}^{P2D}(x_n)}{c_{ss}^{P2D}(x_n)}\right)^2}$$

$$Total\ RMS_{ss}^{model} = \sum_{x} RMS_{ss}^{model}(x)\ ; x \in \left\{0^-, L^-, L^+, 0^+\right\}$$

$$RMS_{e}^{model}(x) = \sqrt{\frac{1}{n}\sum_{n}\left(\frac{c_{e}^{model}(x_n) - c_{e}^{P2D}(x_n)}{c_{e}^{P2D}(x_n)}\right)^2}$$

$$Total\ RMS_{e}^{model} = \sum_{x} RMS_{e}^{model}(x)\ ; x \in \left\{0^-, L^-, L^+, 0^+\right\}$$

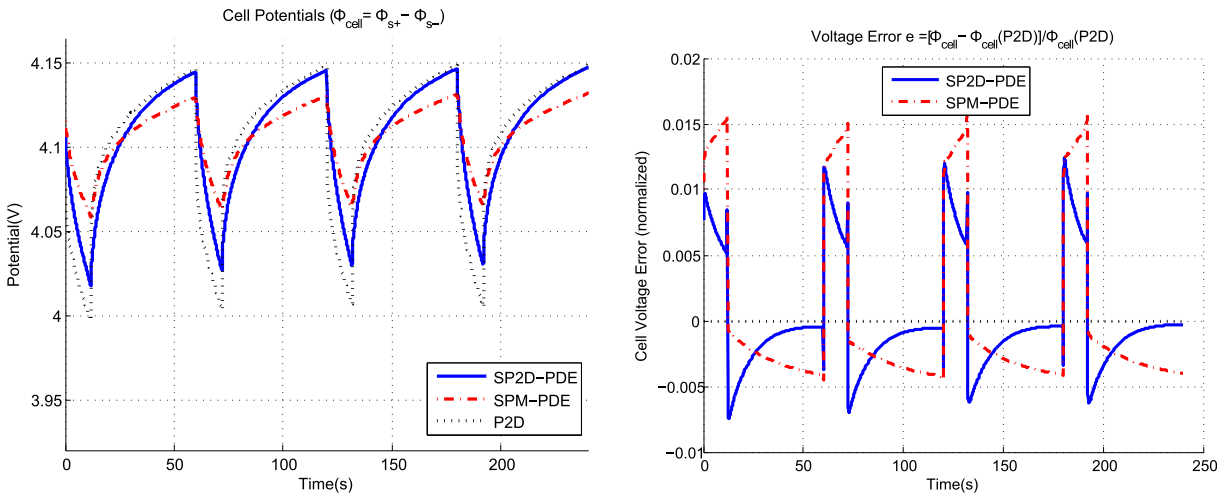

(a) Cell Voltage (b) Normalized Voltage Error

Fig. 7. Voltage output and normalized voltage error of the SPM-PDE and SP2D-PDE versus the P2D model at 4C peak discharge.

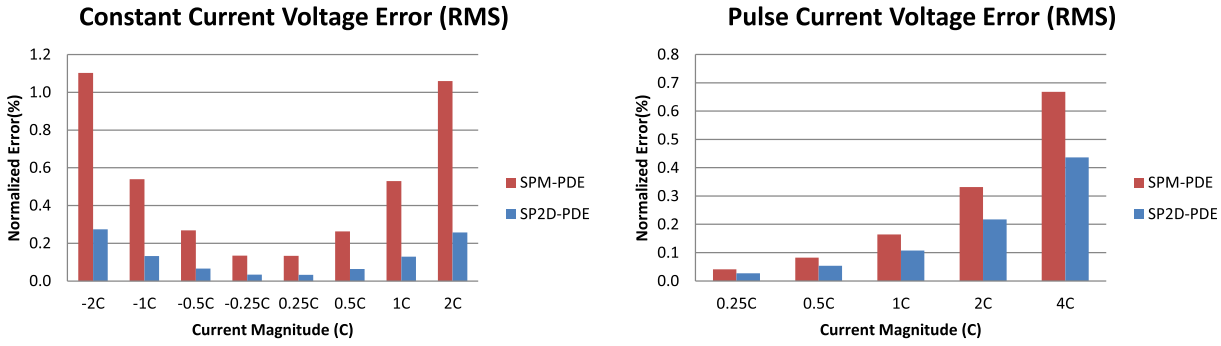

(a) Constant Current (b) Pulse Current

Fig. 8. Summary of the simulations. The RMS error was calculated for voltages higher than 3.0 V, since it is a common threshold for safe cell usage.

Figs. 9–11 plot the models' normalized concentration error as compared to the P2D boundary values. The locus $x = L^-$ was chosen solely for illustration purposes. Fig. 12 summarizes the RMS error sum across all simulations. The detailed data can be found in Tables D.2–D.6.

By examining the concentration error plots, it is effortless to notice that on most cases the concentration predictions from SP2D are more similar to the P2D than those predictions from SPM (which is basically the averaged value). Although one can also find that in a few cases the SPM has a similar or better prediction error on locus $x = L^-$, the total error sum at the four chosen loci is significantly smaller as shown in Fig. 12. In addition, similar to the cell voltage case, the predictions at constant current are more accurate than those obtained at pulse current simulations. The simulations show that, on a general sense, the boundary predictions from SP2D are in agreement with the original P2D model and could be used for more advanced BMS applications such as lithium plating prediction and available power prediction.

5. Prediction of local plating

The model developed in the previous sections benefits from the simplicity of calculating simple averaged models like the SPMs, while being able to generate insights about the inner concentrations analogously to the full order P2D. By knowing the critical values, it is possible to predict safety boundaries of a cell in a dynamic way, and with that information, derive operational limits with higher levels of confidence.

Apart from enabling monitoring of critical values of a cell, this unique performance can also be made useful for real applications: by reducing the computational requirements to predict a single-cell behavior, more cells can be simultaneously observed closer to their safety limits with higher levels of confidence. This section will discuss some of these potential applications and give some examples to illustrate their expected benefits.

5.1. Lithium plating

While the aging of the cells is not completely understood, there has been significant effort to model and understand the key underlying causes [16,19,20,28–30]. One of these phenomena is lithium plating, in which metallic lithium deposits at the surface of the particle [20]. The drawbacks from lithium plating are significant:

- Metallic lithium does not dissolve back into its ionic form easily, thus accounts for capacity fade;

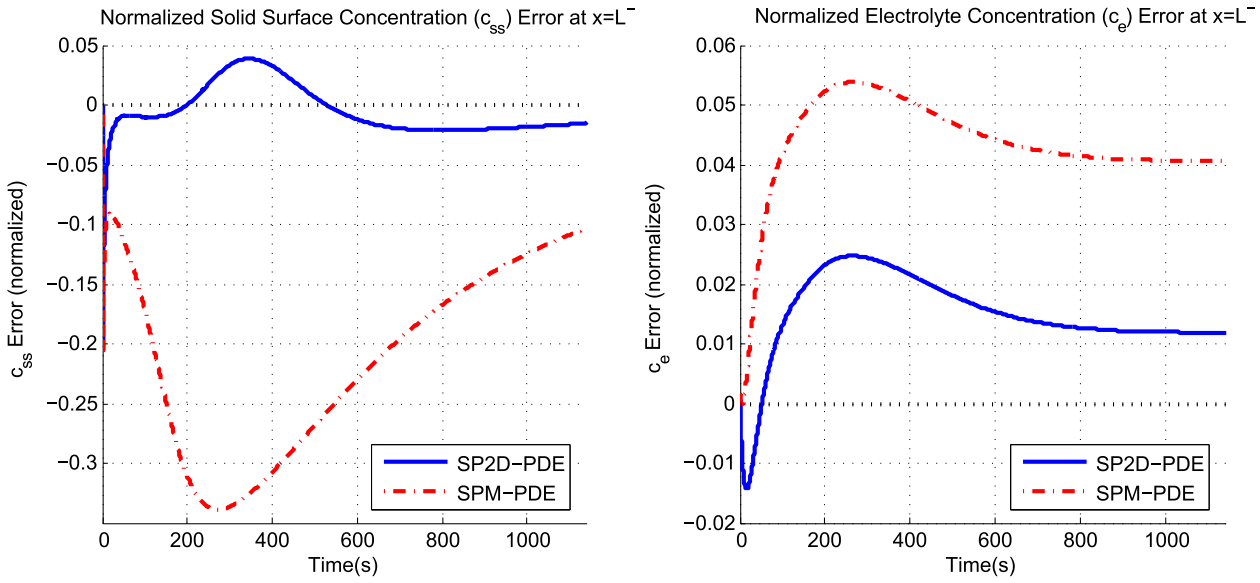

Fig. 9. Solid and electrolyte concentration error at the negative electrode/separator boundary. This data is obtained from the same simulation of Fig. 5.

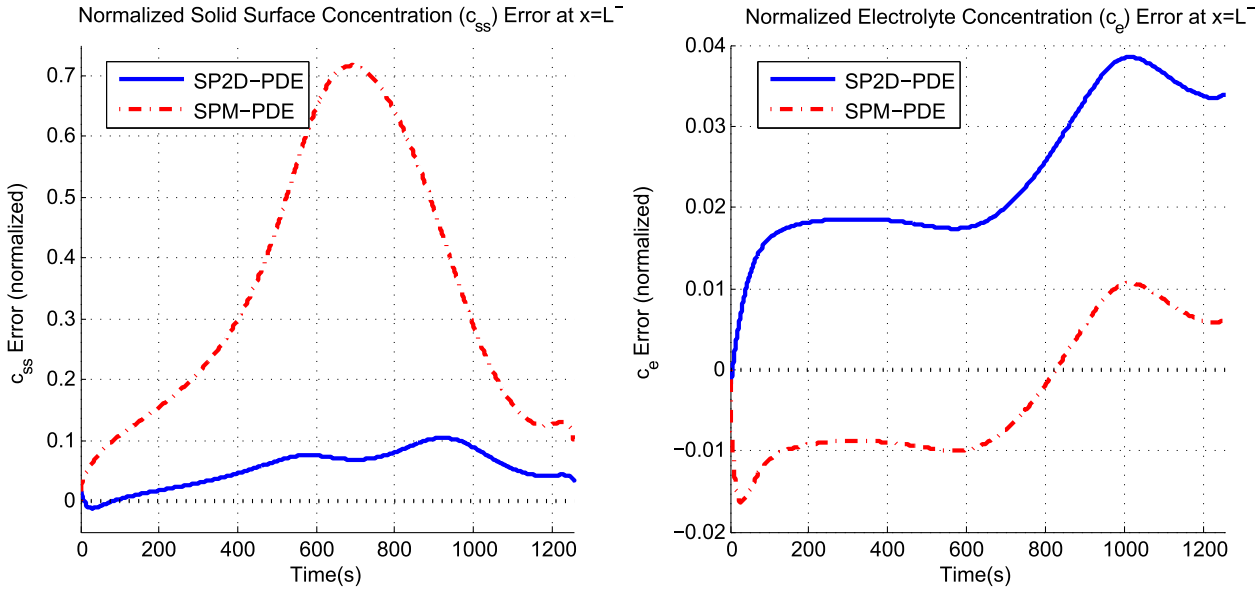

Fig. 10. Solid and electrolyte concentration error at the negative electrode/separator boundary. This data is obtained from the same simulation of Fig. 6.

- With the increase of metallic depositions there is a reduction of available area for lithium intercalation, decreasing the available power and increasing the SEI resistance;
- Lithium plating can also lead to dendrite formation, which in turn can lead to internal shorts.

Lithium plating is a side-reaction and it was not originally included in this model development. However, analogously to [30], it is possible to estimate when the plating will occur by monitoring the plating overpotential. The side-reaction overpotential is defined as:

$$\eta^{sr}(x,t) = \Phi_s(x,t) - \Phi_e(x,t) - \mathscr{U}^{sr}(c_{ss}(x,t)) - R_f^{sr} j_n^{sr}(x,t) \quad (60)$$

It is known that the plating equilibrium potential $\mathscr{U}^{sr}$ is zero and that the flux j_n^{sr} is negligible [4], thus leading to:

$$\eta^{sr}(x,t) \approx \Phi_s(x,t) - \Phi_e(x,t) \quad (61)$$

This simplification enables the BMS to monitor this specific reaction using only the solid and electrolyte potentials which were calculated using SP2D. Lastly, plating will occur when the side-reaction overpotential is lower than zero [4,19,30]:

$$\eta^{sr}(x,t) \leq 0 \rightarrow \Phi_s(x,t) - \Phi_e(x,t) \leq 0 \quad (62)$$

5.2. Simulation

Using the method above, the plating overpotential was estimated for a 2C constant-current charge using P2D, SP2D and the SPM in an aged cell.[9] The simulations were conducted until a standard safety boundary was crossed, i.e., maximum cell voltage

[9] The cell aging was simulated by increasing R_f ten-fold.

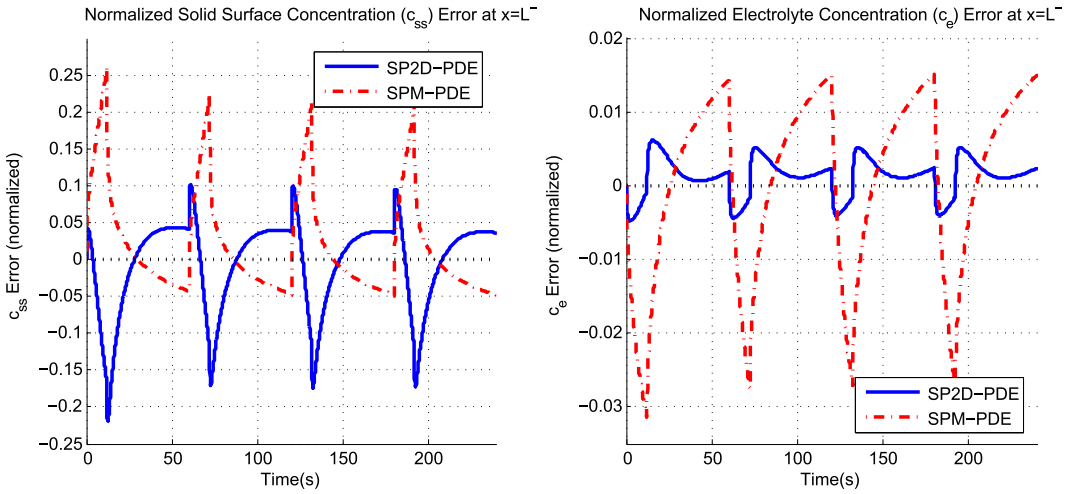

Fig. 11. Solid and electrolyte concentration error at the negative electrode/separator boundary. This data is obtained from the same simulation of Fig. 7.

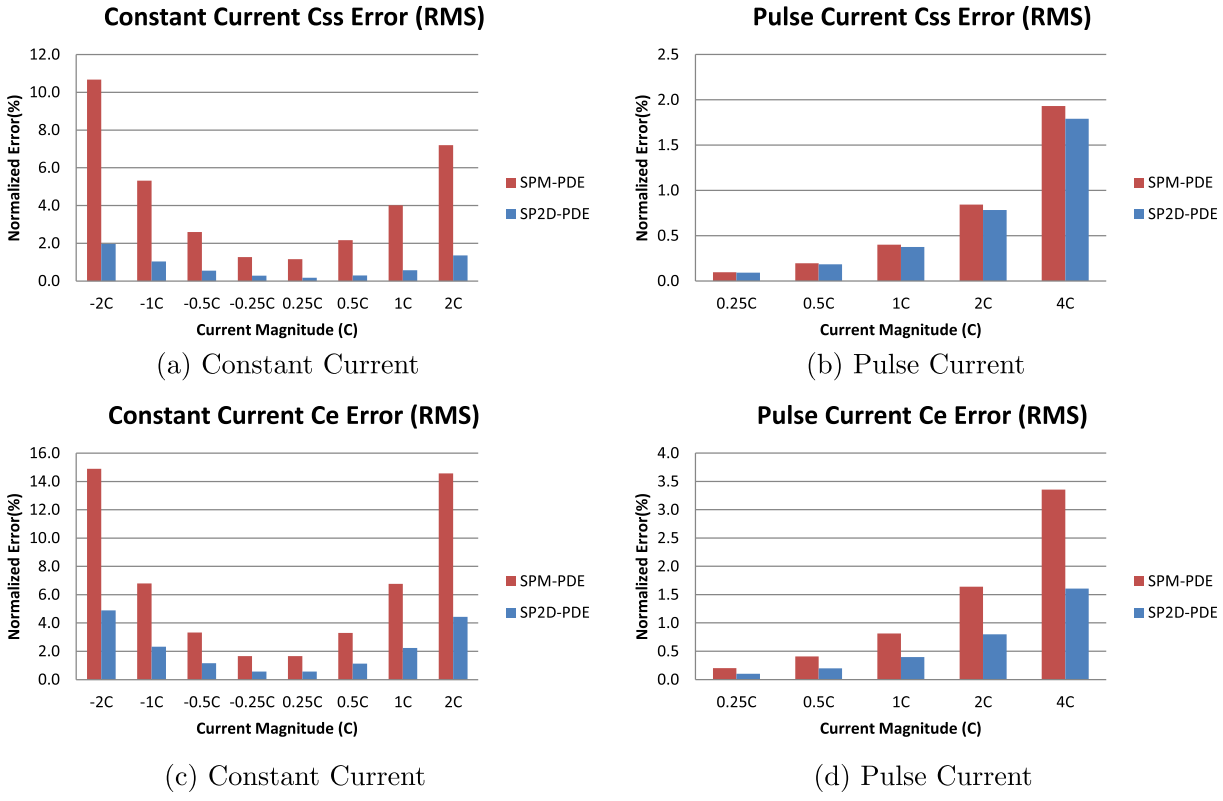

Fig. 12. Summary of the simulations. a and b represent the c_{ss} error. c and d represent the c_e error.

in this case. The cell boundaries were chosen to plot the curves since they usually represent the most extreme values inside of a cell.

Fig. 13 depicts the simulation results. Both P2D and SP2D are able to generate results for the whole cell, whereas the SPM generates only one result per electrode due to its heavy simplifying assumptions. It is possible to notice the necessity for intra-cell gradients: at high currents there is a significant difference between the averaged plating overpotential and the local overpotential at the cell borders. One can observe that the SP2D yields similar predictions to the P2D, whereas the SPM lags significantly before predicting a potentially dangerous operation. This local information is particularly useful to utilize the full potential of the battery (e.g. minimize recharge time and maximizing regeneration capacity) while ensuring the safety of batteries.

6. Concluding remarks

By considering the variation of lithium concentration over the spatial domain, especially at the boundaries between the cell domains, a reduced-order electrochemical battery model is developed. The concentration dynamics are averaged at each cell domain

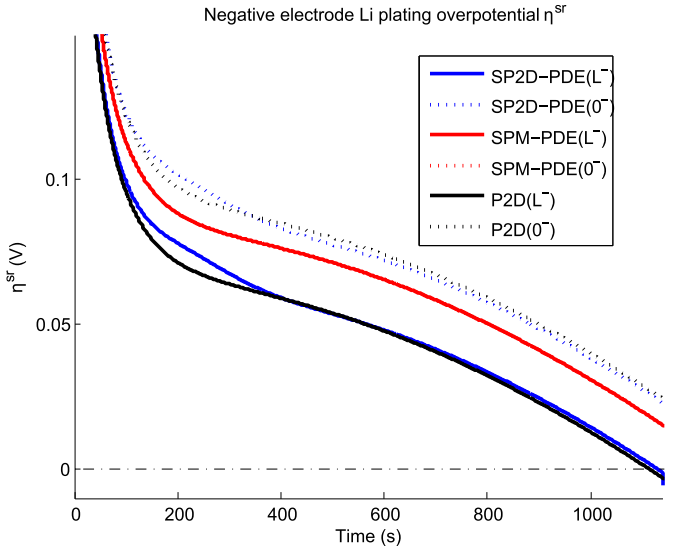

Fig. 13. Lithium plating estimation based on side-reaction overpotential under 2C constant charge. The SPM has constant values across the electrode, thus yielding only the averaged prediction at all points (i.e. both curves are overlapped).

(positive and negative electrodes, and the separator) in order to decouple the dynamics in the solid and electrolyte, as well as to reduce the number of states. Following this, the lithium concentration profile is estimated using the averaged states with the aid of algebraic equations derived from the steady-state P2D model. This step is the key difference between the developed model and existing averaged models including SPM. Finally, the concentration at the boundaries is used to calculate the cell potential, yielding significant accuracy improvements both for pulse charge and for constant current (i.e., RMS error below 0.5% for any of the proposed models in any simulated case).

A key application of the derived model, aside from solely predicting the cell voltage, is presented: lithium plating prediction. It is expected that the employment of the presented model will be of great benefit for BMS, which employs several cells and/or needs to push the cells to their limits.

The presented models can be further improved to accommodate thermal behavior or can be used directly for SOC estimation (e.g., similarly to [15]), or coupled with existing closed-loop observer techniques. Further improvements may additionally include an account of the pore-wall flux density variations over the spatial domain, similar to the concepts presented in Refs. [10,11,18].

Acknowledgments

This work was supported by the National Research Foundation of Korea grant funded by the Ministry of Science, ICT and Future Planning under grant number NRF-2013R1A1A1060397.

Appendix A. SP2D electrolyte potential derivation

Follows the derivation of $\Phi_e(x,t)$. Starting from equation (9), repeated here for convenience:

$$\frac{\partial \Phi_e(x,t)}{\partial x} = -\frac{i_e(x,t)}{\kappa} + \frac{2RTt_a^0}{F}\left(\frac{\partial \ln c_e(x,t)}{\partial x}\right)$$

We proceed to integrate (9) over the x dimension, for each of the domains (i.e. from x = 0 to x = L):

$$\int_0^L \frac{\partial \Phi_e(x,t)}{\partial x}dx = \int_0^L \left[-\frac{i_e(x,t)}{\kappa} + \frac{2RTt_a^0}{F}\left(\frac{\partial \ln c_e(x,t)}{\partial x}\right)\right]dx$$

Since the profile of $i_e(x,t)$ is not known, we rearrange (8) to yield:

$$i_e(x,t) = i(t) + \sigma\frac{\partial \Phi_s(x,t)}{\partial x} \tag{A.1}$$

Lastly, in order to solve the integral, we assume that the electrolyte conductivity coefficient at a given domain is very close to the average value of it on said domain:

$$\kappa(c_e(x,t)) \approx \overline{\kappa}(t) = \kappa\left(\overline{c_e}(t)\right) \tag{A.2}$$

Defining:

$$\Delta f = f(L,t) - f(0,t) \tag{A.3}$$

and using (A.2), we can then solve the integral, leading to:

$$\Delta\Phi_e = -\frac{L}{\overline{\kappa}}i(t) - \frac{\sigma}{\overline{\kappa}}\Delta\Phi_s + \frac{2RTt_a^0}{F}(\Delta \ln c_e)$$

Now plugging in (2), and multiplying all terms by $\overline{\kappa}$:

$$\Delta\Phi_e(\overline{\kappa}+\sigma) = -Li(t) - \sigma(\Delta\eta_s + \Delta\mathscr{U}(c_{ss}) + \Delta\Omega) + \frac{2RTt_a^0}{F}(\Delta \ln c_e)$$

$$\Delta\Phi_e = \frac{-Li(t) - \sigma(\Delta\eta_s + \Delta\mathscr{U}(c_{ss})) + \frac{2RTt_a^0}{F}(\Delta \ln c_e)}{\overline{\kappa}+\sigma} \tag{A.4}$$

Equation (A.4) is the same of (39) and concludes this derivation.

Appendix B. SP2D electrolyte averaged dynamics

The derivation starts from integrating (11) over the x dimension, for each of the domains (i.e. from $x = 0$ to $x = L$):

$$\int_0^L \frac{\partial c_e(x,t)}{\partial t} = \int_0^L \frac{\partial}{\partial x}\left(D_e\frac{\partial c_e(x,t)}{\partial x}\right) + \int_0^L \frac{t_a^0}{F\varepsilon}\frac{\partial i_e(x,t)}{\partial x}$$

$$\int_0^L \frac{\partial c_e(x,t)}{\partial t} = D_e\left(\left.\frac{\partial c_e(x,t)}{\partial x}\right|_{x=L} - \left.\frac{\partial c_e(x,t)}{\partial x}\right|_{x=0}\right) + \frac{t_a^0}{F\varepsilon}\left(i_e(x,t)|_{x=L} - i_e(x,t)|_{x=0}\right) \tag{B.1}$$

At this point, let's recall the definition of averaged concentration:

$$\overline{c_e}(t) = \frac{1}{L}\int_0^L c_e(x,t)dx$$

Using Leibniz integral rule, acknowledging that the boundaries don't vary with time, and using the above expression, (B.1) becomes:

$$\frac{d}{dt}\overline{c_e}(t) = \frac{D_e}{L}\left(\frac{\partial c_e(x,t)}{\partial x}\Big|_{x=L} - \frac{\partial c_e(x,t)}{\partial x}\Big|_{x=0}\right) + \frac{t_a^0}{F\varepsilon L}\left(i_e(x,t)|_{x=L} - i_e(x,t)|_{x=0}\right) \tag{B.2}$$

Following, the boundary conditions are applied, which leads to:

$$\frac{d}{dt}\overline{c_e^+}(t) = \frac{D_e}{L^+}\left(\frac{\partial c_e(x,t)}{\partial x}\Big|_{x=L^+}\right) + \frac{t_a^0}{F\varepsilon^+ L^+} i^+(t) \tag{B.3}$$

$$\frac{d}{dt}\overline{c_e^{sep}}(t) = \frac{D_e}{\varepsilon^{sep}L^{sep}}\left(-\varepsilon^+\frac{\partial c_e(x,t)}{\partial x}|_{x=L^+} - \varepsilon^-\frac{\partial c_e(x,t)}{\partial x}|_{x=L^-}\right) \tag{B.4}$$

$$\frac{d}{dt}\overline{c_e^-}(t) = \frac{D_e}{L^-}\left(\frac{\partial c_e(x,t)}{\partial x}\Big|_{x=L^-}\right) + \frac{t_a^0}{F\varepsilon^- L^-} i^-(t) \tag{B.5}$$

Equations (B.3–B.5) require the concentration variation at the separator boundaries to be evaluated. In order to obtain the concentration variation at the boundaries, the estimated concentration profiles (48) and (50) are differentiated with respect to x:

$$\frac{\partial}{\partial x}\widehat{c_e^+}(x,t) = -\frac{2x}{\varepsilon^+ L^+}\left(\overline{c_e^+}(t) - c_e^0\right)\left(\gamma^+ - \frac{L^+}{3\varepsilon^+}\right)^{-1} \tag{B.6}$$

$$\frac{\partial}{\partial x}\widehat{c_e^-}(x,t) = -\frac{2x}{\varepsilon^- L^-}\left(\overline{c_e^-}(t) - c_e^0\right)\left(\gamma^- - \frac{L^-}{3\varepsilon^-}\right)^{-1} \tag{B.7}$$

Plugging (B.6) and (B.7) into (B.3–B.5):

$$\frac{d}{dt}\overline{c_e^+}(x,t) = \frac{D_e}{\varepsilon^+ L^+}\left(c_e^0 - \overline{c_e^+}(x,t)\right)\left(\gamma^+ - \frac{L^+}{3\varepsilon^+}\right)^{-1} + \frac{t_a^0}{F\varepsilon^+ L^+} i^+(t) \tag{B.8}$$

$$\frac{d}{dt}\overline{c_e^{sep}}(x,t) = -\frac{2D_e}{L^{sep}}\left[\left(c_e^0 - \overline{c_e^+}(x,t)\right)\left(\gamma^+ - \frac{L^+}{3\varepsilon^+}\right)^{-1} + \left(c_e^0 - \overline{c_e^-}(x,t)\right)\left(\gamma^- - \frac{L^-}{3\varepsilon^-}\right)^{-1}\right] \tag{B.9}$$

$$\frac{d}{dt}\overline{c_e^-}(x,t) = \frac{D_e}{\varepsilon^- L^-}\left(c_e^0 - \overline{c_e^-}(x,t)\right)\left(\gamma^- - \frac{L^-}{3\varepsilon^-}\right)^{-1} + \frac{t_a^0}{F\varepsilon^- L^-} i^-(t) \tag{B.10}$$

Equations (B.8)–(B.10) are equal to (51)–(53), thus concluding this derivation. Using a simple change of variables (e.g. $u(t) = \overline{c_e}(x,t) - c_e^0$), the resulting system becomes a linear system and can be evaluated effortlessly.

Appendix C. Potential formulas at boundaries

These formulas were derived using the same process described in Ref. [25].

The electrolyte potential equations at the boundaries can be derived using the previously derived (A.4). Evaluating (A.4), using (12) and (17), for the positive electrode domain:

$$\Phi_e|_{x=L^+} = \frac{-L^+ I(t) - \sigma^+\left(\Delta\eta_s^+ + \Delta\mathscr{U}^+\right) + \frac{2RTt_a^{0+}\overline{\kappa^+}}{F}\Delta\ln c_e^+}{\overline{\kappa^+} + \sigma^+} \tag{C.1}$$

Next, evaluating (A.4), using (12) and (18), for the separator domain:

$$\Phi_e|_{x=L^-} = \Phi_e|_{x=L^+} - \left[\frac{L^{sep} I(t)}{\overline{\kappa^{sep}}} + \frac{2RTt_a^{0sep}}{F}\Delta\ln c_e^{sep}\right] \tag{C.2}$$

Lastly, evaluating (A.4), using (12), for the negative electrode domain:

$$\Phi_e|_{x=0^-} = \Phi_e|_{x=L^-} - \left[\frac{L^- I(t) - \sigma^-\left(\Delta\eta_s^- + \Delta\mathscr{U}^-\right) + \frac{2RTt_a^{0-}\overline{\kappa^-}}{F}\Delta\ln c_e^-}{\overline{\kappa^-} + \sigma^-}\right] \tag{C.3}$$

The open circuit potential $\mathscr{U}(c_{ss})$ is simply:

$$\mathscr{U}(c_{ss})|_x = \mathscr{U}(c_{ss}(x)) \tag{C.4}$$

The ohmic losses are approximated using an averaged pore-wall flux density:

$$\Omega(x,t) = FR_f j_n(x,t) \approx FR_f\overline{j_n}(t) \tag{C.5}$$

There are also no significant changes to (5) besides expressing it in terms of average pore-wall flux density $\overline{j_n}(t)$ and the estimated exchange current density $\widehat{i_0}(t)$:

$$\eta_s(x,t) = \frac{2RT}{F}\operatorname{arcsinh}\left(\frac{F\overline{j_n}(t)}{\widehat{i_0}(x,t)}\right) \tag{C.6}$$

where the estimated exchange current density at the boundary is defined as:

$$\widehat{i_0}(x,t) = Fk_{eff}\sqrt{\widehat{c_e}(x,t)\widehat{c_{ss}}(x,t)\left(c_s^{max} - \widehat{c_{ss}}(x,t)\right)} \tag{C.7}$$

Appendix D. Simulation result tables

Tables D.1 to D.6 summarize the simulation results for full charge and full discharge, at various constant current inputs.

Table D.1
Voltage RMS error of SPM-PDE and SP2D-PDE vs P2D model at constant current simulations.

Input current	Voltage RMS error (%)		Abs. compared to SPM (%)
	SPM PDE	SP2D PDE	SP2D PDE
−2C	1.103	0.273	−75.2
−1C	0.540	0.132	−75.6
−C/2	0.269	0.066	−75.3
−C/4	0.134	0.034	−74.9
C/4	0.133	0.033	−75.6
C/2	0.263	0.064	−75.8
1C	0.529	0.129	−75.6
2C	1.059	0.257	−75.7

Table D.2
Solid surface concentration total RMS error of SPM-PDE and SP2D-PDE vs P2D model at constant current simulations.

Input current	c_{ss} RMS error (%)		Abs. compared to SPM (%)
	SPM PDE	SP2D PDE	SP2D PDE
−2C	14.90	4.899	−67.1
−1C	6.799	2.332	−65.7
−C/2	3.332	1.152	−65.4
−C/4	1.659	0.574	−65.4
C/4	1.659	0.569	−65.7
C/2	3.303	01.122	−66.0
1C	6.768	2.240	−66.9
2C	14.58	4.438	−69.6

Table D.3
Electrolyte concentration total RMS error of SPM-PDE and SP2D-PDE vs P2D model at constant current simulations.

Input current	c_e RMS error (%)		Abs. compared to SPM (%)
	SPM PDE	SP2D PDE	SP2D PDE
−2C	10.68	1.970	−81.6
−1C	5.313	1.032	−80.6
−C/2	2.591	0.551	−78.7
−C/4	1.272	0.282	−77.8
C/4	1.152	0.171	−85.1
C/2	2.168	0.293	−86.5
1C	4.010	0.570	−85.8
2C	7.199	1.355	−81.2

Table D.4
Voltage RMS error of SPM-PDE and SP2D-PDE vs P2D for pulse current.

Input current	Voltage RMS error (%)		Abs. compared to SPM (%)
	SPM PDE	SP2D PDE	SP2D PDE
0.25C	0.041	0.027	−34.9
0.5C	0.082	0.053	−34.9
1C	0.164	0.107	−34.7
2C	0.331	0.217	−34.5
4C	0.668	0.437	−34.6

Table D.5
Solid surface concentration total RMS Error of SPM-PDE and SP2D-PDE vs P2D for pulse current.

Input current	c_{ss} RMS error (%)		Abs. compared to SPM (%)
	SPM PDE	SP2D PDE	SP2D PDE
0.25C	0.203	0.100	−50.8
0.5C	0.406	0.199	−50.9
1C	0.814	0.399	−51.3
2C	1.639	0.798	−51.3
4C	3.354	1.608	−52.1

Table D.6
Electrolyte concentration total RMS Error of SPM-PDE and SP2D-PDE vs P2D for pulse current.

Input current	c_e RMS error (%)		Abs. compared to SPM (%)
	SPM PDE	SP2D PDE	SP2D PDE
0.25C	0.097	0.091	−6.06
0.5C	0.195	0.184	−5.84
1C	0.399	0.374	−6.35
2C	0.842	0.782	−7.10
4C	1.932	1.791	−7.30

Appendix E. Simulation parameters, equations and nomenclature

Table E.7 summarizes the parameters used in the simulations.

Table E.7
List of parameters used on the simulation.

Symbol	Positive	Separator	Negative
Chemistry	$LiCoO_2$	–	LiC_6
c_e^0	1000		
c_s^{max}	51,217	–	24,983
D_e	4.5807×10^{-11}	2.7877×10^{-10}	4.5807×10^{-11}
D_s	1×10^{-13}	–	4×10^{-14}
k_{eff}	4.5×10^{-6}	–	9.71×10^{-6}
L	1×10^{-4}	2.5×10^{-5}	1×10^{-4}
R_f*	0	0	1×10^{-3}
R_p	1×10^{-5}	–	1×10^{-5}
t_a^0	0.6	0.6	0.6
T	298		
V_{cell}^{min}	2.0		
V_{cell}^{max}	4.47		
ε	0.3	1	0.3
ε_f	0.2	0	0.1
ρ	1.25×10^{-2}	–	9.8×10^{-2}
σ_∞	10	–	100
For full charge simulation			
c_s^0	$0.84 \times c_s^{max-}$	–	$0.02 \times c_s^{max+}$
For full discharge simulation			
c_s^0	$0.28 \times c_s^{max-}$	–	$0.97 \times c_s^{max+}$
For pulse charge simulation			
c_s^0	$0.5 \times c_s^{max-}$	–	$0.6 \times c_s^{max+}$

No marks: parameter from Ref. [26]; *: parameter from Ref. [9].

The positive open circuit potential function, as defined in Ref. [26]:

$$\mathscr{U}^+\left(c_{ss}^+\right) = 4.825510 - 0.950237\exp\left[-\left(\frac{\nu - 0.913511}{0.600492}\right)^2\right];$$
$$\nu = c_{ss}^+ \Big/ c_s^{max+} \tag{E.1}$$

The negative open circuit potential function, as defined in Ref. [26]:

$$\mathscr{U}^-\left(c_{ss}^-\right) = 0.7222 + 0.1386\delta + 0.028952\delta^{0.5} - 0.017189\delta^{-1} + 0.0019144\delta^{-1.5} + 0.28082\exp(0.9 - 15\delta) - 0.79844\exp(0.44649(\delta - 0.92));$$
$$\delta = c_{ss}^- \Big/ c_s^{max-} \tag{E.2}$$

The electrolyte conductivity coefficient equation [26]:

$$\kappa_\infty = \left(0.0911 + 1.9101\gamma - 1.052\gamma^2 + 0.1554\gamma^3\right); \gamma = c_e/1000 \tag{E.3}$$

Lastly, Table E.8 summarizes the nomenclature used in this paper.

Table E.8
Nomenclature for this paper.

Symbol	Name (units)
a	Specific interfacial area (m^{-1})
c_e	Lithium concentration on electrolyte (mol m^{-3})
c_s	Lithium concentration on electrode (mol m^{-3})
c_s^{max}	Max. lithium concentration on electrode (mol m^{-3})
c_{ss}	Lithium concentration on particle surface (mol m^{-3})
D_e	Diffusion coefficient on electrolyte (m^2 s^{-1})
D_s	Diffusion coefficient on electrode (m^2 s^{-1})
F	Faraday's constant (96,487 C mol^{-1})
i	Total current density (A m^{-2})
i_e	Electrolyte current density (A m^{-2})
i_s	Electrode current density (A m^{-2})
i_0	Exchange current density (A m^{-2})
$I(t)$	Input current density (A m^{-2})
j_n	Pore-wall flux density (mol m^{-2} s^{-1})
k_{eff}	Intercalation rate constant ($m^{2.5}$ $mol^{-0.5}$ s^{-1})
L	Thickness of domain (m)
q	Concentration flux on solid (mol m^{-4})
R	Gas constant (8.314 J mol^{-1} K^{-1})
R_f	SEI film resistance (Ω m^2)
R_p	Solid particle radius (m)
t_a^0	Anion transference number (−)
T	Cell temperature (K)
$\mathscr{U}(c_{ss})$	Open-circuit potential (V)
ε	Electrolyte volume fraction (−)
ε_f	Inert filler volume fraction (−)
η_s	Electrode overpotential (V)
κ	Electrolyte ionic conductivity (S m^{-1})
ρ	Fitting variable (−)
σ	Electrode conductivity (S m^{-1})
Φ_e	Electrolyte potential (V)
Φ_s	Electrode potential (V)

Appendix F. Supplementary data

Supplementary data related to this article can be found at http://dx.doi.org/10.1016/j.jpowsour.2015.03.134.

References

[1] D.L. Thomas, B. Reddy (Eds.), Linden's Handbook of Batteries, fourth ed., McGraw Hill, 2010.

[2] P.W. Northrop, B. Suthar, V. Ramadesigan, S. Santhanagopalan, R.D. Braatz, V.R. Subramanian, Efficient simulation and reformulation of lithium-ion battery models for enabling electric transportation, J. Electrochem. Soc. 161 (8) (2014) E3149–E3157.

[3] M. Lawder, B. Suthar, P. Northrop, S. De, C. Hoff, O. Leitermann, M. Crow, S. Santhanagopalan, V. Subramanian, Battery energy storage system (bess) and battery management system (bms) for grid-scale applications, Proc. IEEE 102 (6) (2014) 1014–1030, http://dx.doi.org/10.1109/JPROC.2014.2317451.

[4] N. Chaturvedi, R. Klein, J. Christensen, J. Ahmed, A. Kojic, Algorithms for advanced battery-management systems, Control Syst. IEEE 30 (3) (2010) 49–68, http://dx.doi.org/10.1109/MCS.2010.936293.

[5] T. Hansen, C.-J. Wang, Support vector based battery state of charge estimator, J. Power Sources 141 (2) (2005) 351–358, http://dx.doi.org/10.1016/j.jpowsour.2004.09.020. http://www.sciencedirect.com/science/article/pii/S0378775304010626.

[6] W. Junping, G. Jingang, D. Lei, An adaptive Kalman filtering based state of charge combined estimator for electric vehicle battery pack, Energy Convers. Manag. 50 (12) (2009) 3182–3186, http://dx.doi.org/10.1016/j.enconman.2009.08.015. http://www.sciencedirect.com/science/article/pii/S0196890409003240.

[7] C. Fleischer, W. Waag, Z. Bai, D.U. Sauer, On-line self-learning time forward voltage prognosis for lithium-ion batteries using adaptive neuro-fuzzy inference system, J. Power Sources 243 (2013) 728–749.

[8] V.R. Subramanian, V.D. Diwakar, D. Tapriyal, Efficient macro-micro scale coupled modeling of batteries, J. Electrochem. Soc. 152 (10) (2005) A2002–A2008, http://dx.doi.org/10.1149/1.2032427. http://jes.ecsdl.org/content/152/10/A2002.full.pdf+html. http://jes.ecsdl.org/content/152/10/A2002.abstract.

[9] V.R. Subramanian, V. Boovaragavan, V.D. Diwakar, Toward real-time simulation of physics based lithium-ion battery models, Electrochem. Solid-State Lett. 10 (11) (2007) A255–A260, http://dx.doi.org/10.1149/1.2776128. http://esl.ecsdl.org/content/10/11/A255.full.pdf+html. http://esl.ecsdl.org/content/10/11/A255.abstract.

[10] S.K. Rahimian, S. Rayman, R.E. White, Extension of physics-based single particle model for higher charge–discharge rates, J. Power Sources 224 (0) (2013) 180–194, http://dx.doi.org/10.1016/j.jpowsour.2012.09.084. http://www.sciencedirect.com/science/article/pii/S0378775312015054.

[11] X. Han, M. Ouyang, L. Lu, J. Li, Simplification of physics-based electrochemical model for lithium ion battery on electric vehicle. Part ii: Pseudo-two-dimensional model simplification and state of charge estimation, J. Power Sources 278 (2015) 814–825.

[12] L. Cai, R.E. White, Reduction of model order based on proper orthogonal decomposition for lithium-ion battery simulations, J. Electrochem. Soc. 156 (3) (2009) A154–A161, http://dx.doi.org/10.1149/1.3049347. http://jes.ecsdl.org/content/156/3/A154.full.pdf+html. http://jes.ecsdl.org/content/156/3/A154.abstract.

[13] C.Y. Wang, W.B. Gu, B.Y. Liaw, Micromacroscopic coupled modeling of batteries and fuel cells: I. Model development, J. Electrochem. Soc. 145 (10) (1998) 3407–3417, http://dx.doi.org/10.1149/1.1838820. http://jes.ecsdl.org/content/145/10/3407.full.pdf+html. http://jes.ecsdl.org/content/145/10/3407.abstract.

[14] Di Domenico Domenico, Stefanopoulou Anna, Fiengo Giovanni, Lithium-ion battery state of charge and critical surface charge estimation using an electrochemical model-based extended Kalman filter, J. Dyn. Syst. Meas. Control 132(6).

[15] E. Prada, D. Di Domenico, Y. Creff, J. Bernard, V. Sauvant-Moynot, F. Huet, Simplified electrochemical and thermal model of lifepo4-graphite Li-ion batteries for fast charge applications, J. Electrochem. Soc. 159 (9) (2012) A1508–A1519, http://dx.doi.org/10.1149/2.064209jes. http://jes.ecsdl.org/content/159/9/A1508.full.pdf+html. http://jes.ecsdl.org/content/159/9/A1508.abstract.

[16] E. Prada, D. Di Domenico, Y. Creff, J. Bernard, V. Sauvant-Moynot, F. Huet, A simplified electrochemical and thermal aging model of lifepo4-graphite Li-ion batteries: power and capacity fade simulations, J. Electrochem. Soc. 160 (4) (2013) A616–A628, http://dx.doi.org/10.1149/2.053304jes. http://jes.ecsdl.org/content/160/4/A616.full.pdf+html. http://jes.ecsdl.org/content/160/4/A616.abstract.

[17] G. Ning, B.N. Popov, Cycle life modeling of lithium-ion batteries, J. Electrochem. Soc. 151 (10) (2004) A1584–A1591, http://dx.doi.org/10.1149/1.1787631. http://jes.ecsdl.org/content/151/10/A1584.full.pdf+html. http://jes.ecsdl.org/content/151/10/A1584.abstract.

[18] W. Luo, C. Lyu, L. Wang, L. Zhang, A new extension of physics-based single particle model for higher charge–discharge rates, J. Power Sources 241 (0) (2013) 295–310, http://dx.doi.org/10.1016/j.jpowsour.2013.04.129. http://www.sciencedirect.com/science/article/pii/S0378775313007398.

[19] Z. Li, J. Huang, B. Yann Liaw, V. Metzler, J. Zhang, A review of lithium deposition in lithium-ion and lithium metal secondary batteries, J. Power Sources 254 (2014) 168–182.

[20] M. Petzl, M.A. Danzer, Nondestructive detection, characterization, and quantification of lithium plating in commercial lithium-ion batteries, J. Power Sources 254 (2014) 80–87.

[21] K.E. Thomas, J. Newman, R.M. Darling, Mathematical modeling of lithium batteries, in: W. Schalkwijk, B. Scrosati (Eds.), Advances in Lithium-ion Batteries, Springer, US, 2002, pp. 345–392, http://dx.doi.org/10.1007/0-306-47508-1-13. http://dx.doi.org/10.1007/0-306-47508-1-13.

[22] M. Doyle, T.F. Fuller, J. Newman, Modeling of galvanostatic charge and discharge of the lithium/polymer/insertion cell, J. Electrochem. Soc. 140 (6) (1993) 1526–1533, http://dx.doi.org/10.1149/1.2221597. http://jes.ecsdl.org/content/140/6/1526.full.pdf+html. http://jes.ecsdl.org/content/140/6/1526.abstract.

[23] T.F. Fuller, M. Doyle, J. Newman, Simulation and optimization of the dual lithium ion insertion cell, J. Electrochem. Soc. 141 (1) (1994) 1–10, http://dx.doi.org/10.1149/1.2054684. http://jes.ecsdl.org/content/141/1/1.full.pdf+html. http://jes.ecsdl.org/content/141/1/1.abstract.

[24] J. Newman, K.E. Thomas-Alyea, Electrochemical Systems, third ed., John Wiley & Sons, 2012.

[25] P. Kemper, Lithium-ion Battery Electrochemical Model for High-current Control Applications- Extended Single Particle Model (Master's thesis), KAIST, 2014, http://library.kaist.ac.kr/thesis02/2014/2014M020124317_S1Ver1.pdf.

[26] J. Newman, Dualfoil 5.1, Newmans Research group webpage, http://www.cchem.berkeley.edu/jsngrp/.

[27] P. Kemper, D. Kum, Extended single particle model of li-ion batteries towards high current applications, in: Vehicle Power and Propulsion Conference (VPPC), 2013, IEEE, 2013, pp. 1–6, http://dx.doi.org/10.1109/VPPC.2013.6671682.

[28] S. Zhang, K. Xu, T. Jow, Study of the charging process of a $LiCoO_2$-based Li-ion battery, J. Power Sources 160 (2) (2006) 1349–1354.

[29] M.B. Pinson, M.Z. Bazant, Theory of sei formation in rechargeable batteries: capacity fade, accelerated aging and lifetime prediction, J. Electrochem. Soc. 160 (2) (2013) A243–A250, http://dx.doi.org/10.1149/2.044302jes. http://jes.ecsdl.org/content/160/2/A243.full.pdf+html. http://jes.ecsdl.org/content/160/2/A243.abstract.

[30] N. Legrand, B. Knosp, P. Desprez, F. Lapicque, S. Raël, Physical characterization of the charging process of a li-ion battery and prediction of Li plating by electrochemical modelling, J. Power Sources 245 (2014) 208–216.